Orientation Selective Recrystallization of Nonoriented Electrical Steels

L. KESTENS, J.J. JONAS, P. VAN HOUTTE, and E. AERNOUDT

A nonoriented electrical steel that was commercially hot rolled and then given a 70 pct cold reduction on a laboratory mill was annealed at 680 °C for 6 minutes. The sheet was then submitted to a second rolling reduction of 5.2 pct, followed in turn by a second annealing at 730 °C for various times. The textures were measured after the first and second recrystallization treatments and analyzed using a nucleation and growth model. In the model, the nucleus orientation distribution function is first calculated by assessing the nucleation probability for each deformed matrix orientation. The nucleation texture is then transformed into the recrystallization texture by means of an appropriate growth criterion. The calculations indicate that the annealing texture of the conventionally rolled (70 pct reduction) sheet can be accounted for on the basis of random nucleation followed by selective growth. The latter is characterized by the following physical features: (a) the low mobility of low angle grain boundaries, (b) the enhanced mobility of {110} plane matching boundaries, and (c) variant selection of the {110} plane that carries the largest amount of slip during deformation. The computer simulations also show that low stored energy nucleation is favored in the lightly rolled sheet. These nuclei grow into the matrix by a selection mechanism that involves the increased mobility of Σ19a and Σ33a ⟨110⟩ coincident site lattice (CSL) boundaries.

I. INTRODUCTION

THE development of primary recrystallization textures in low and extra low carbon steels has been studied predominantly in deep drawing steels.[1] Texture control has also been widely investigated in grain oriented electrical steels.[2] In the latter case, the final texture is obtained by a secondary recrystallization treatment that gives rise to a very sharp Goss component ({110}⟨001⟩). Much less is known, however, about texture development in nonoriented (NO) electrical steels. Nevertheless, it is clear that a very sharp Goss component is inappropriate, as it is associated with highly favorable magnetic properties that are restricted to the rolling direction. Because NO electrical steels are used mainly as magnetic flux carriers in small electric motors, the magnetic properties should ideally be equally good in all directions, and not only in the rolling direction. The most appropriate texture for NO electrical steels is, therefore, a cubic fiber texture in which all grains have a ⟨001⟩ axis parallel to the normal direction (ND) of the sheet. Such a texture averages out the number of easily magnetized ⟨001⟩ directions in the plane of the sheet.

The development of annealing textures can be explained in terms of oriented nucleation and selective growth, and supporting evidence has been cited for both mechanisms.[3] Recently, a quantitative model has been proposed,[4,5] in which the main features of oriented nucleation and selective growth are taken into account. In this model, it is assumed that the orientation dependence of the stored energy can be described accurately by the Taylor factors of the individual orientations. This led to a nucleation probability function that depends only on the Taylor factors of the deformed grains. Furthermore, selective growth was implemented in the model by assigning a growth probability to each nucleus orientation. This probability is assumed to be a function of the average crystallographic misorientation between a particular nucleus orientation and the surrounding deformed matrix.

According to Watanabe,[6] growth is favored when a nucleus and a matrix grain have a ⟨110⟩ axis in common, *i.e.*, when the {110} "plane matching" condition is fulfilled. This theory of selective growth differs from the widely discussed coincident site lattice (CSL) mechanism[7] in that the former only requires a common rotation axis for a given nucleus-matrix grain pair, without any insistence on a particular misorientation angle. The origin of the increased mobility of the high angle boundaries between {110} plane matched grains can be attributed to their lower free volumes compared with *random* high angle boundaries. The volume expansion per unit area $\delta V/A_0$ of the ⟨110⟩ plane matching boundaries is only about 4 pct of the lattice parameter, whereas, it is in the range of 12.5 to 25 pct for boundaries between ⟨100⟩ rotated grains, as well as for the boundaries between grains of unrelated orientations.[8,9] Such "low expansion boundaries" are able to accommodate a smaller proportion than other boundaries of the impurity atoms that cause solute drag.

The model proposed by Kestens and Jonas[4] allows for the addition of a variant selection criterion to the growth law. This rule was derived empirically by Tóth and Jonas[10,11] from their dynamic recrystallization experiments on fcc materials; it was later found to apply to observations on static recrystallization in interstitial-free (IF) steels (*i.e.*, bcc materials) by Urabe and Jonas.[12] The rule states that the misorientation axis perpendicular to the most active slip plane of the deformed matrix grain plays a favored role

L. KESTENS, Research Associate, is with the Department of Flat Rolling, Centre for Research in Metallurgy, B-9052 Gent, Belgium. J.J. JONAS, Professor, is with the Department of Metallurgical Engineering, McGill University, Montreal, PQ, Canada H3A 2A7. P. VAN HOUTTE, Professor, and E. AERNOUDT, Professor, are with the Department of Metallurgy and Materials Engineering, Katholieke Universiteit Leuven, B-3001, Belgium.

Manuscript submitted October 27, 1995.

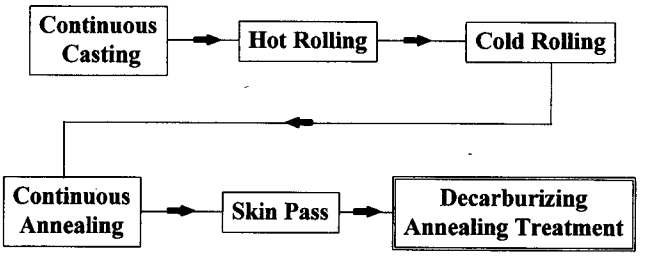

Fig. 1—Conventional thermomechanical processing of NO electrical steels.

Table I. Composition of the Nonoriented Electrical Steel (Mass Pct)

C	Mn	Si	P	S	N_2	Al_{met}
0.010	0.229	0.395	0.118	0.001	0.0031	0.338

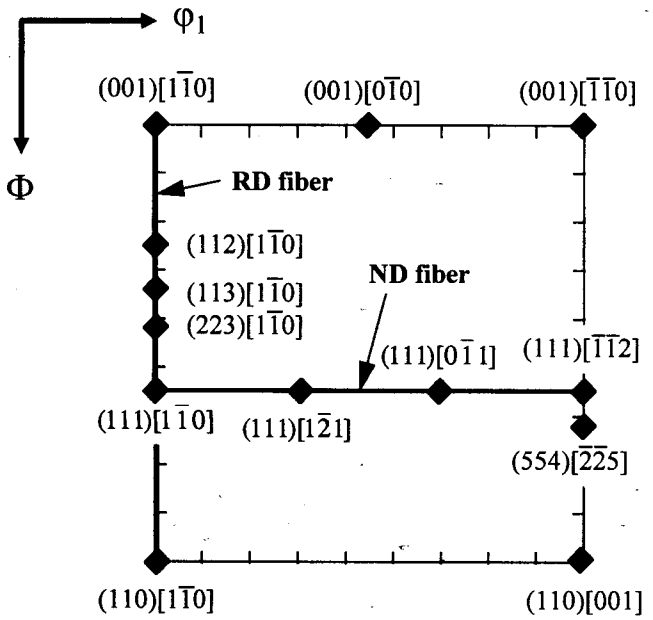

Fig. 2—φ_2 = 45 deg section of Euler space showing the ideal bcc rolling and recrystallization components.

during growth selection. There is a link between the plane matching observations of Watanabe[6] and the variant selection rule of Urabe and Jonas[12] in that the {110} planes are also important slip planes in bcc materials. The variant selection rule has a physical basis in the stimulated diffusion of solutes along the dislocation arrays that form on the active slip planes. Because the geometry of the bcc lattice requires the ⟨110⟩ rotation axis to be approximately perpendicular to the dislocation arrays that lie in or near the {110} planes, such accelerated diffusion has the effect of increasing the mobility of tilt and near-tilt boundaries, due to the fact that they are perpendicular to the pipe diffusion planes.[12]

In previous publications,[4,5,13] the oriented nucleation and selective growth model was used successfully to calculate the annealing textures of two distinct IF steels. In this article, the model is employed to account for the textures produced by two successive combinations of rolling and annealing carried out on an NO electrical steel. The model is also used as a tool for the quantitative analysis of the experimental data. In this way, it was possible to assess various hypotheses concerning the occurrence of alternative recrystallization mechanisms.

II. EXPERIMENTAL

The industrial processing of the less expensive grades of NO electrical steels does not differ widely from the conventional processing of unalloyed low carbon steels. A flow chart of the successive thermomechanical treatments employed in the commercial manufacture of these steels is presented in Figure 1. For the higher quality grades, a decarburizing treatment is applied as the final processing step. The coarser grain sizes and lower carbon contents produced by this annealing treatment are mainly responsible for the improved magnetic properties.

In order to simulate the final stages of processing, a commercially hot-rolled sheet was cold rolled on a laboratory mill in 15 passes, leading to an accumulated reduction of 70 pct. The composition of the steel is given in Table I. The presence of alloying elements (Si, Mn, Al, and P) has the effect of minimizing magnetic losses. After cold reduction, the material was given a first annealing treatment in a salt bath at 680 °C for 6 minutes. Subsequently, a second, but very light, rolling reduction of 5.2 pct was applied in a single pass. This second cold working operation was followed by a second annealing treatment at 730 °C. Samples were extracted from the salt bath after 1, 2, 4, 8, 16, 30, and 60 minutes. The second reduction, together with the second annealing treatment, simulates the skin pass followed by the decarburization anneal employed in industrial practice. A large number of comparative tests[14] indicated that such laboratory treatments produce microstructural as well as textural features that are representative of the industrial process.

After each processing step, the microstructures were evaluated by optical metallography. Four incomplete pole figures ({110}, {200}, {211}, and {310}) were measured on a SIEMENS* D500 texture goniometer. The orientation distribution functions (ODFs) were then calculated from these pole figures using the software developed by Van Houtte.[15]

*SIEMENS is a trademark of Siemens Electrical Equipment, Toronto.

III. RESULTS

For convenience, the textures of rolled or annealed bcc materials are frequently represented in the φ_2 = 45 deg section of Euler space. In contrast with the conventional pole figure representation of textures, this particular ODF section identifies the individual fiber components that are present without any ambiguity whatsoever. For reference later, the important components of bcc rolling and annealing textures are illustrated on a φ_2 = 45 deg section of Euler space in Figure 2. The textures measured after hot rolling, the first cold rolling, and the first annealing treatment are presented in Figures 3(a) through (c), respectively. The hot-rolled texture (Figure 3(a)) is quite sharp, with a maximum intensity of 27.5 at the rotated cube position ({001}⟨110⟩). After cold rolling (Figure 3(b)), the maxi-

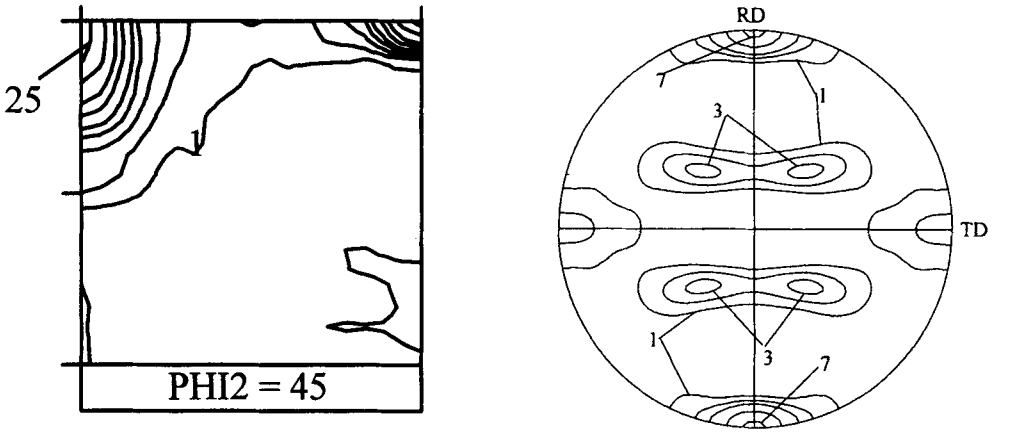

(*a*)

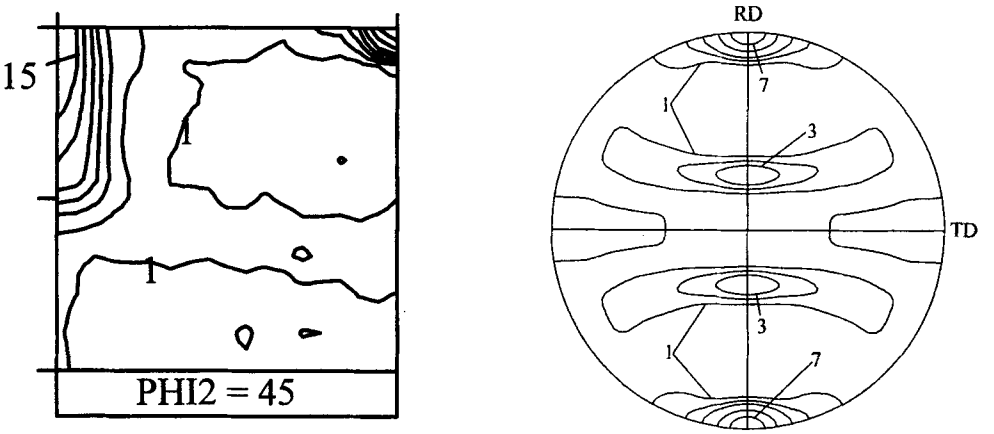

(*b*)

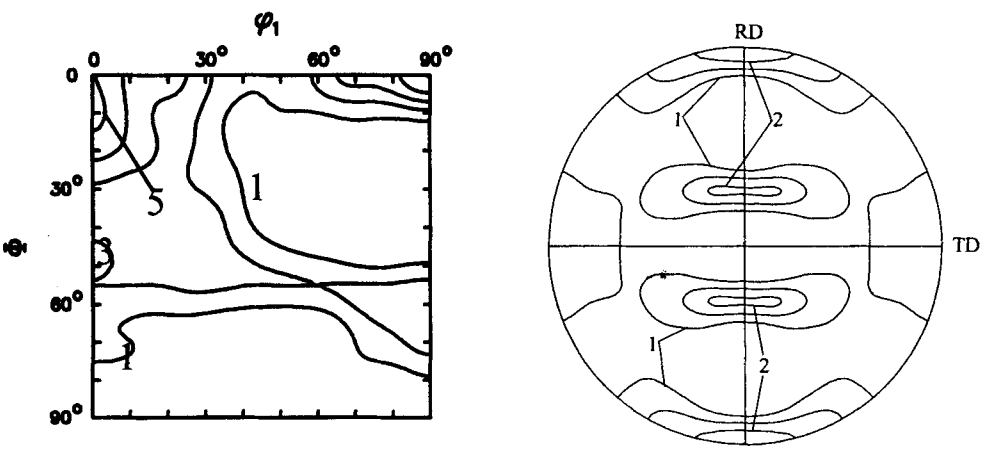

(*c*)

Fig. 3—(*a*) φ_2 = 45 deg section and {110} pole figure of the experimental hot rolling texture (levels of the ODF section: 1-3-5-7-9-12-15-20-25; max = 27.5). (*b*) φ_2 = 45 deg section and {110} pole figure of the experimental cold rolling texture (levels of the ODF section: 1-3-5-7-9-12-15; max = 19.5). (*c*) φ_2 = 45 deg section and {110} pole figure of the experimental annealing texture. Note that the intervals here are twice as frequent as in Figs. (a) and (b) (levels of the ODF section: 1-2-3-4-5; max = 5.2).

mum is spread out somewhat along the rolling direction (RD) fiber (⟨110⟩ // RD), although the absolute maximum (19.5) remains at the {001}⟨110⟩ component. A weak ND fiber (⟨111⟩ // ND) also develops during cold rolling. It is evident from Figure 3(c) that considerable orientation change occurs during the first annealing treatment, leading to a pronounced weakening of the texture. The randomizing effect of recrystallization is clearly illustrated by the sharp drop in the maximum intensity from a high of 19.5 to 5.2 after the annealing treatment.

Metallographic examination after the second annealing treatment revealed that recrystallization was triggered at the surface of the sheet. Grains grow from the surface and gradually progress toward the center, as can be seen on the micrographs of Figures 4(a) through (c), respectively, after 4, 8, and 60 minutes of annealing. In order to assess the

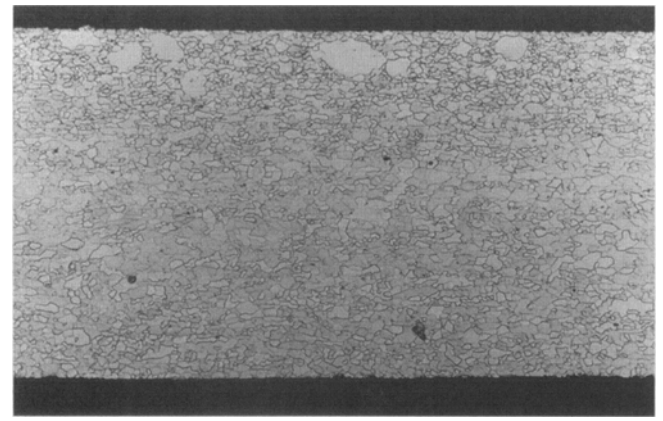

(*a*)

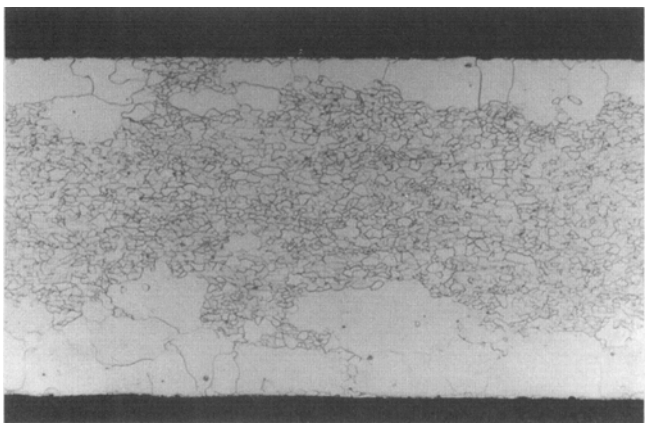

(*b*)

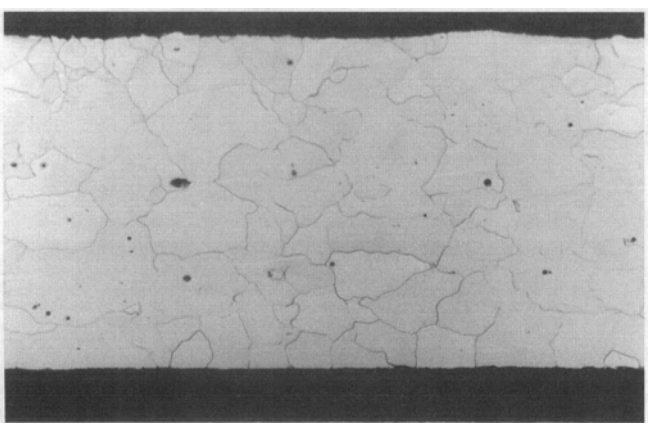

(*c*)

Fig. 4—Microstructure of cold-rolled sample (with 5.2 pct reduction) after second annealing at 730 °C for (*a*) 4 min, (*b*) 8 min, and (*c*) 60 min.

nature of the observed growth, an additional sample was annealed at 730 °C for 60 minutes but without the preceding cold reduction of 5.2 pct. The microstructural examination of this sample indicated that directional growth of the type displayed by the rolled sample was absent in this case. This confirmed that the driving force for the grain growth event was the deformation energy supplied by the light rolling reduction and that true primary recrystallization took place. The onset of recrystallization at the surface can be attributed to the strain gradient developed during single-pass rolling.

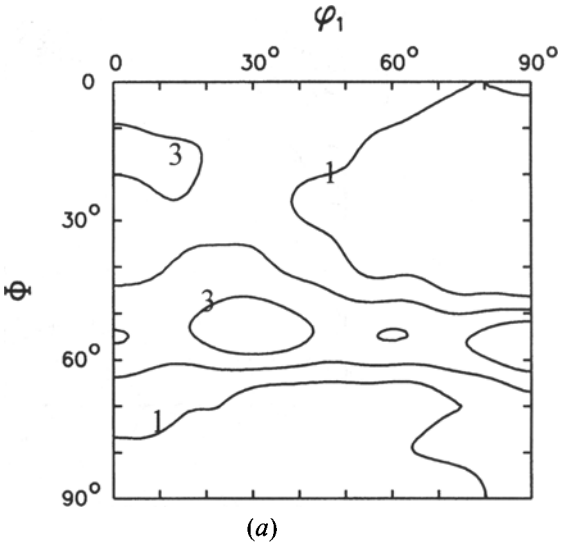

(*a*)

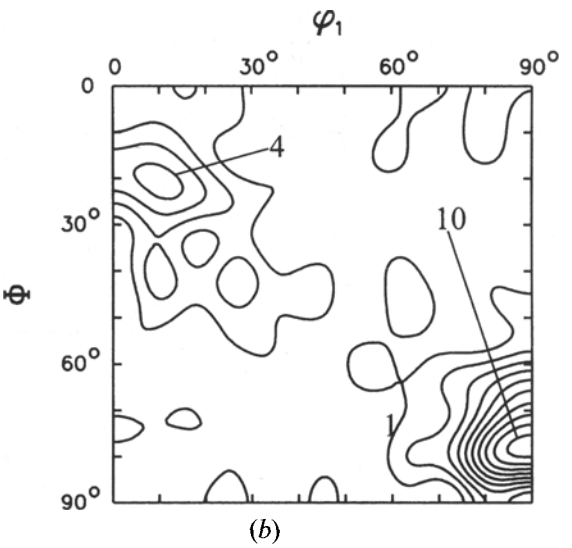

(*b*)

Fig. 5—Experimental (surface) textures after (*a*) 5.2 pct rolling reduction (max = 4.0) and (*b*) after annealing (max = 10.8) (levels: 1-2-3-4-5-6-7-8-9-10).

Due to the nature of the second recrystallization and owing to the suspected presence of texture gradients, it was decided that only surface textures would be compared before and after annealing. This is because these are the only ones for which the topological origin is unambiguously known. The annealed surface texture undoubtedly originates from the rolled surface texture, whereas the cold-rolled layer from which the annealed midlayer texture originates is not quite clear. Only surface textures will, therefore, be evaluated after the second annealing treatment.

Figure 5(a) shows the skin pass texture at the surface after a reduction of 5.2 pct. It resembles the first recrystallization texture at the surface because a reduction of 5.2 pct is too slight to have a pronounced effect on the orientation distribution. Comparison of Figures 5(a) and 3(c) (midlayer texture after the first annealing treatment) indicates that a texture gradient is present after the first an-

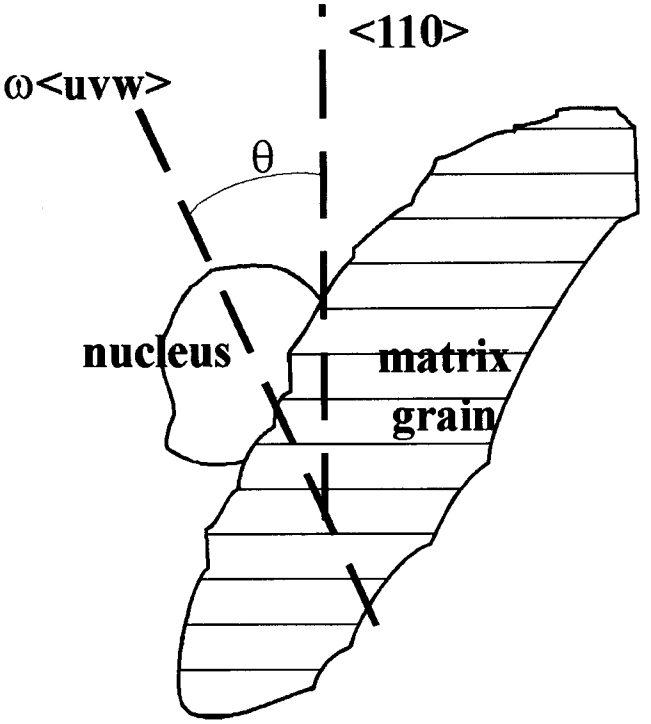

Fig. 6—Schematic representation of the misorientation between an arbitrary combination of a nucleus and a matrix grain. Here, ω ⟨*uvw*⟩ represents the misorientation axis and angle linking the nucleus to the matrix grain. The ⟨110⟩ axis that is identified is perpendicular to the most active slip plane in the matrix grain.

nealing treatment, because the ND fiber is more pronounced at the surface (Figure 5(a)) than in the midlayer (Figure 3(c)). At the end of the second annealing treatment (after 60 minutes of holding), the texture attains the features shown in Figure 5(b). Two maxima appear: a local maximum of 4 near {114}⟨110⟩ and the absolute maximum of 10 at {441}⟨118⟩, which is 10 deg away from the Goss component ({110}⟨001⟩).

IV. MODELING OF THE ANNEALING TEXTURES

A. *General Scope of the Model*

The model employed in this investigation has already been described in detail by Kestens and Jonas[4] so that it will only be reviewed briefly here. The basic assumption of the method is that the process of recrystallization can be modeled in two sequential steps: a nucleation stage followed by a separate growth stage. Throughout the calculations, a discrete set of Q orientations g_i, each of volume fraction $F(g_i)$, is used to represent the overall orientation distribution function. The individual orientations and their volume fractions are derived from the continuous ODF $f(g)$ by employing a suitable discretization procedure[16]

$$F(g_i) = \int_{\Delta g_i} f(g)\, dg \qquad [1]$$

with Δg_i a finite environment around the discrete orientation g_i.

The selection of particular orientations during nucleation is described by the function $P_N(g_i)$, which specifies the probability that a matrix orientation g_i will generate a nucleus of the same orientation. The overall nucleation texture $F^N(g_i)$ is thus obtained by multiplying this probability $P_N(g_i)$ by the deformation texture $F^D(g_i)$

$$F^N(g_i) = c_1 P_N(g_i) F^D(g_i) \qquad [2]$$

The factor c_1 is employed here to facilitate normalization of the nucleation texture to unity.

In the second stage of the calculation, the probability $P_G(g_i)$ that a particular nucleus orientation g_i will grow into the deformed matrix must be assessed. This is calculated by averaging the local growth probabilities $P_L(g_i, g_j)$, where g_j represents the set of matrix orientations. Each individual value of P_L specifies the probability that a given nucleus g_i will grow into a particular matrix orientation g_j. In the model, it is assumed that the local growth probability depends solely on the crystallographic misorientation Δg_{ij} between the nucleus and the matrix grain. Since all matrix orientations g_j contribute to the average growth probability with weight factors given by their respective volume fractions $F^D(g_j)$, the average growth probability can simply be expressed as follows, with c_2 as a normalization constant

$$P_G(g_i) = c_2 \sum_{j=1}^{Q} F^D(g_j) P_L(\Delta g_{ij}) \qquad [3]$$

Finally, the recrystallization texture $F^R(g_i)$ is obtained by allowing the growth probability function $P_G(g_i)$ to operate on the nucleation texture $F^N(g_i)$:

$$F^R(g_i) = c_3 (P_G(g_i))^p F^N(g_i) \qquad [4]$$

where c_3 is the appropriate normalization factor. In Eq. [4], a growth amplification exponent p has been introduced so that the relative importance of oriented nucleation and selective growth can be varied at will.

The specific forms of the nucleation and growth probabilities $P_N(g_i)$ and $P_G(g_i)$, respectively, are functions of the particular nucleation and growth mechanisms that are presumed to operate during recrystallization. These depend on the processing conditions, as will be seen in the examples treated subsequently.

B. *Recrystallization after a Conventional Rolling Reduction (70 Pct)*

It is evident from the experimental results (*i.e.*, comparison of Figures 3(b) and (c)) that recrystallization led to a significant reduction in the sharpness of the texture. In order to simulate this phenomenon, random nucleation was first assumed to take place. This mechanism can, however, be considered to act in two different ways. On the one hand, one can imagine that there are no preferred orientations whatsoever in the nucleation texture. In this case, which will be referred to here as type A, the nucleation texture is truly uniform and $F^N(g)$ = constant. On the other hand, it is also possible to assume that there is no orientation selectivity during nucleation, so that all orientations of the deformation texture have the same nucleation probability $P_N(g)$ = constant. In this case $F^N(g) = F^D(g)$, according to Eq. [2]. This second interpretation will be entitled type B.

The randomly oriented nuclei (whether type A or B) were subsequently submitted to growth competition according to the formalism expressed by Eq. [3]. In accordance

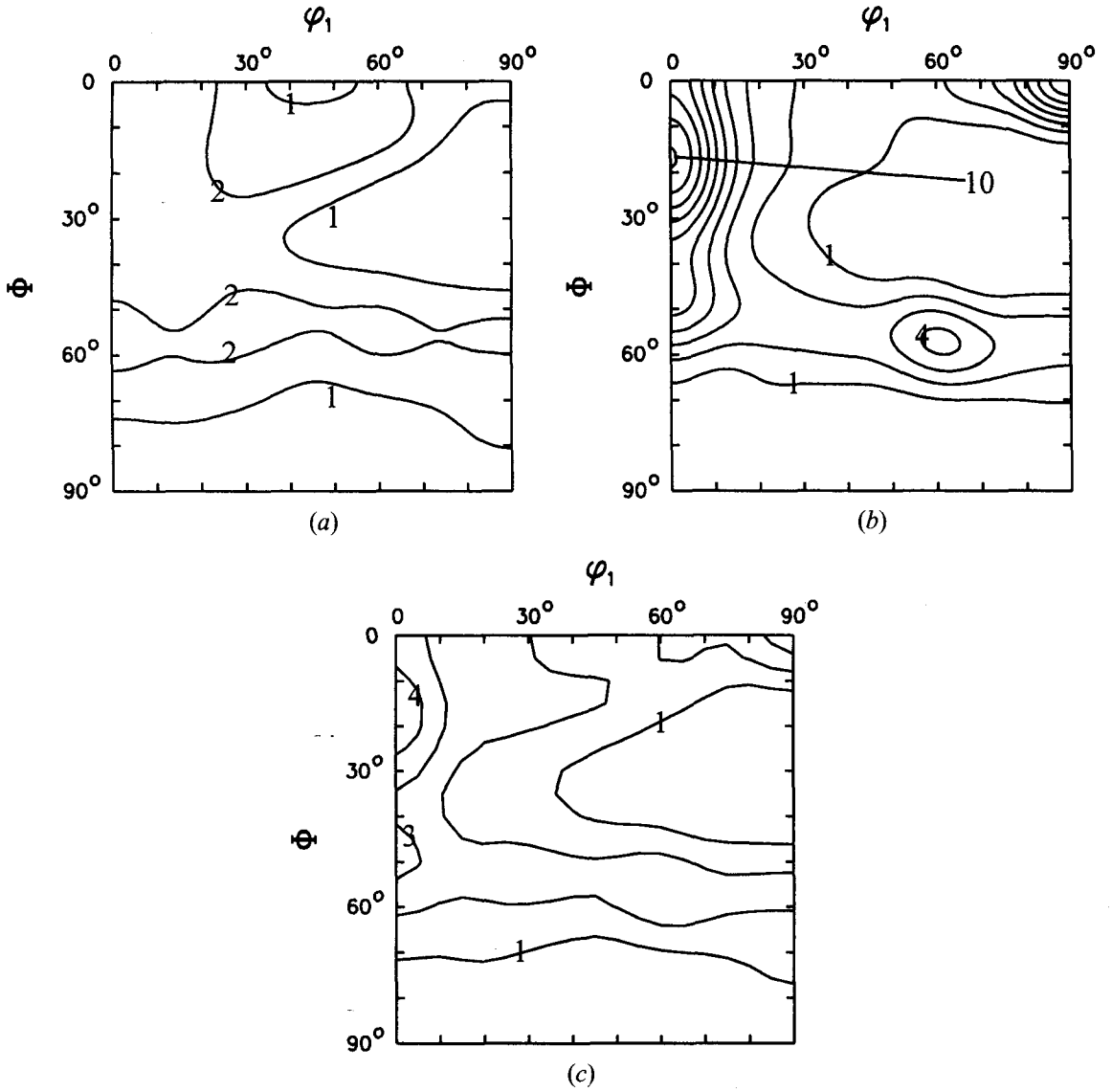

Fig. 7—(*a*) Recrystallization texture simulated using random nucleation ($F^N(g)$ = constant) and selective growth. (*b*) Recrystallization texture simulated using $F^N(g) = F^D(g)$ and selective growth. (*c*) Recrystallization texture obtained by combining the models of Figs. (a) and (b) on the basis of a weight factor of 2:1 (levels: 1-2-3-4-5-6-7-8-9-10).

with the observations of Watanabe,[6] the local growth probability $P_L(\Delta g)$ was designed to favor the growth of {110} plane matching nuclei into the surrounding matrix. Furthermore, the variant selection principle of References 10 through 12 was employed, according to which the most active slip plane of the deformed grain provides the plane involved in the matching (out of six symmetrically equivalent {110} planes). And finally, the restricted mobility of low angle grain boundaries was also taken into account. All these features of orientation dependent selective growth were combined in the following expression for the local growth law, where the coefficient c_4 is the normalization constant of the probability distribution

$$\omega < \omega_0 \qquad P_L(\Delta g_{ij}) = 0 \qquad [5]$$

$$\omega \geq \omega_0 \qquad P_L(\Delta g_{ij}) = c_4 \exp\left[-\left(\frac{\theta_{ij}}{\theta_0}\right)^2\right]$$

In Eq. [5], P_L expresses the probability that a given nucleus orientation will grow into a particular matrix orientation when the nucleus and matrix orientations are linked by the misorientation angle-axis pair $\omega\ \langle uvw \rangle$. Figure 6 represents an arbitrary nucleus-matrix orientation pair, related by an angle-axis pair $\omega\ \langle uvw \rangle$. Of the 24 symmetrically equivalent possibilities for the misorientation axis $\langle uvw \rangle$, the one closest to the $\langle 110 \rangle$ axis perpendicular to the most active slip plane of the deformed matrix grain is chosen. The angle θ_{ij} represents the misorientation between the $\langle uvw \rangle$ axis defined in this way and the $\langle 110 \rangle$ axis concerned. Here, the θ dependence of growth is described by a Gaussian function of characteristic width θ_0.

The recrystallization texture calculated using Eq. [4], with type A random nucleation ($F^N(g)$ = constant) and $p = 1$, is shown in Figure 7(a). This orientation distribution was derived by employing the previous growth criterion (Eqs. [3] and [5] with $\omega_0 = 20$ deg and $\theta_0 = 2$ deg) on the deformation texture displayed in Figure 3(b). It can be seen that, although the simulation bears some resemblance to the experimental annealing texture (Figure 3(c)), it is not completely satisfactory. When the same growth criterion is em-

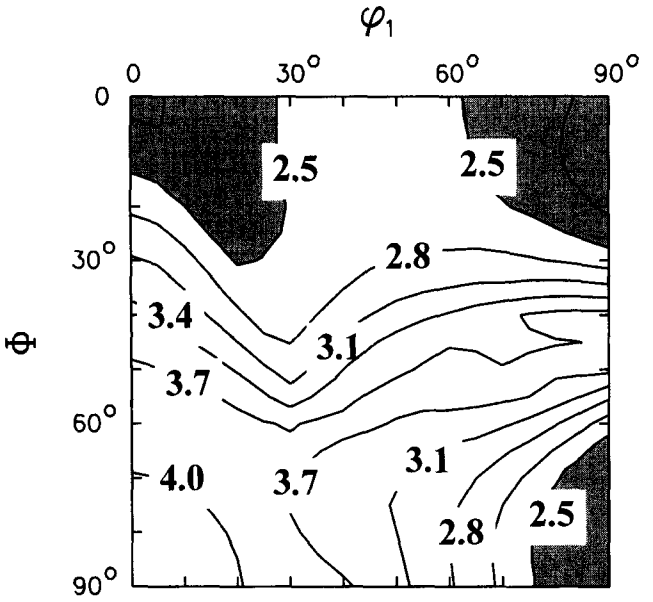

Fig. 8—Taylor factor map calculated on the basis of a lath-type relaxed constraint model.

ployed with exactly the same parameter settings, but with type B nucleation ($F^N(g) = F^D(g)$), the result given in Figure 7(b) is obtained. This texture is still unsatisfactory. However, when the two types of random nucleation are combined with weight factors of 67 pct for type A and 33 pct for type B, the ODF of Figure 7(c) is produced. This simulation leads to an acceptable representation of the experimental texture.

C. *Recrystallization after a Light Rolling Reduction (5.2 Pct)*

In this case, the texture was transformed by the second annealing treatment (60 minutes at 730 °C) after the sheet was submitted to a single rolling pass of 5.2 pct reduction. By comparing the experimental results (Figure 5(b)) with the Taylor factor map of Figure 8, it is evident that the orientations belonging to the low Taylor factor regions of Euler space have been nucleated. This is consistent with the strain induced boundary migration (SIBM) mechanism, which favors the nucleation of orientations with low stored energies.[17] In order to simulate this type of behavior, the following very simple nucleation criterion was employed, which assumes that the Taylor factor of an orientation can be regarded as a measure of its stored energy:

$$\begin{aligned} M > M_0 \quad &: \quad P_N(g_j) = 0 \\ M \leq M_0 \quad &: \quad P_N(g_j) = c_5 \end{aligned} \qquad [6]$$

These relations specify that when the Taylor factor M of a matrix orientation g_j exceeds a critical threshold M_0, the orientation is unable to generate a nucleus. Conversely, all matrix orientations whose Taylor factors fall below this critical limit contribute to nucleation with a constant probability c_5. (This type of dependence is discussed in more detail in Section V–A.) The nucleation ODF derived from the deformation texture of Figure 5(a) by applying the criterion of Eq. [6] with $M_0 = 2.5$ is displayed in Figure 9(a).

The M factors in this example were calculated using the full constraint theory of crystal plasticity by means of a software package available at McGill University.[18] The nucleation textures were also calculated on the basis of the relaxed constraint plasticity models.[19] Use of the lath model, which relaxes the E_{13} component of the strain tensor, leads to the prediction of Figure 9(b). The pancake model, in which the components E_{13} and E_{23} are relaxed, gives rise to the ODF of Figure 9(c). (Here, the 1, 2, and 3 directions refer to the rolling, transverse, and normal directions, respectively.) Although the nucleation texture derived using the lath model bears the closest resemblance to the experimental recrystallization texture (Figure 5(b)), the correspondence is unsatisfactory, which led to the conclusion that the nucleation texture is modified by some subsequent growth selection.

In this case, the growth stage of recrystallization was simulated by applying the same growth criterion (Eq. [5]) as for the conventionally rolled sheet, except that the variant selection rule was abandoned here. The physical justification for the rule, discussed in detail in References 4 and 12, is based on the planar dislocation arrays present in the substructure of 70 pct cold reduced IF steels.[20] Such dislocation structures are unlikely to develop in the present very lightly rolled material (5.2 pct reduction). According to Gil Sevillano *et al.*,[21] for example, well-defined cell structures are only formed in bcc iron when the true strain exceeds 10 pct.

In order to assess the influence of the threshold value M_0, simulations with different M_0 maxima were carried out. The recrystallization textures predicted using M_0 limits of 2.3, 2.5, 2.7, 3.0, and 3.3 are illustrated in Figures 10(a) through (e), respectively. In all these examples, the relaxed constraint lath model ($E_{13} \neq 0$) was employed to calculate the Taylor factors, as the best agreement with the experimental data was obtained in this way. It is evident that the value of M_0 has a critical influence, as it can be seen in Figures 10(c) through (e) that the predictions do not match the experimental results (Figure 5(b)) when $M_0 > 2.5$. The calculations, therefore, suggest that $M_0 = 2.5$ represents an upper stored energy limit for SIBM nucleation.

V. DISCUSSION

A. *The Nucleation Textures*

1. *Random nucleation*

Both the experimental results, as well as the simulations, suggest that a powerful randomizing process dominates orientation selection during annealing after the first rolling reduction. For fcc materials, randomization during annealing has often been related to particle stimulated nucleation (PSN). In the case of bcc materials, however, much less attention has been paid to PSN, although a recent publication by Hutchinson and Ryde[22] mentions PSN as one of the nucleation mechanisms observed during the annealing of cold-rolled steels. Due to the particular chemistries and processing parameters associated with NO electrical steels, PSN cannot be ruled out *a priori*. Table I shows that alloying elements such as Al, Mn, and P were added (mainly to increase the resistivity and, hence, to decrease the eddy current losses). It, therefore, seems reasonable to expect that precipitates will be present in the microstructure in the form of nitrides, sulfides, and phosphides, respectively. Further-

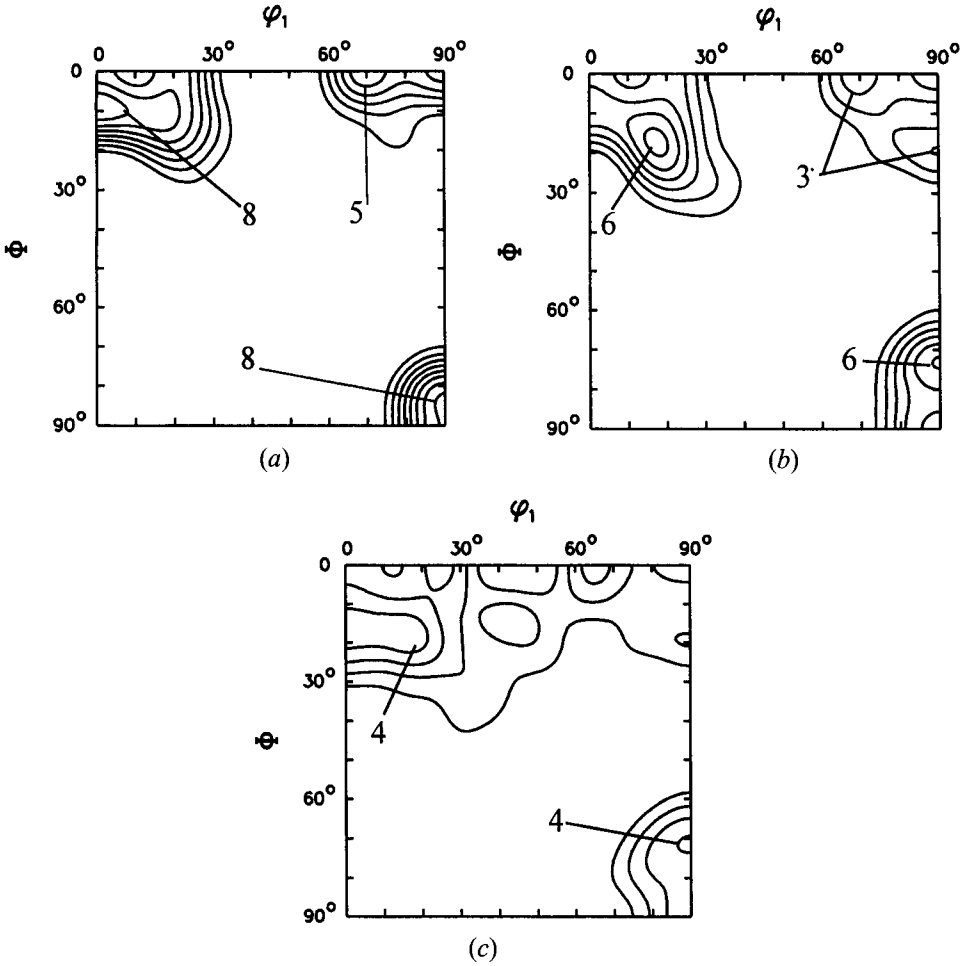

Fig. 9—(*a*) Nucleation texture simulated using Eqs. [2] and [6], with $F^D(g)$ given by the deformation texture of Fig. 5(a) and $M_0 = 2.5$. Here, the M factors were calculated according to the full constraint theory. (*b*) Nucleation texture simulated using Eqs. [2] and [6], with $F^D(g)$ given by the deformation texture of Fig. 5(a) and $M_0 = 2.5$. Here, the M factors were calculated according to the relaxed constraint lath model. (*c*) Nucleation texture simulated using Eqs. [2] and [6], with $F^D(g)$ given by the deformation texture of Fig. 5(a) and $M_0 = 2.5$. Here, the M factors were calculated according to the relaxed constraint pancake model (levels: 1-2-3-4-5-6-7-8).

more, the processing of such steels is aimed at coarsening the precipitates as much as possible, because a coarse precipitate distribution is less detrimental to the magnetic properties than a fine one. Moreover, the presence of (coarse) grain boundary cementite in the hot band can also give rise to randomization of the annealing texture, as revealed by Inagaki.[23]

In a recent article by De Paepe *et al.*,[24] the hot band microstructure of an NO steel, similar to the one of interest here, was investigated. This study revealed the presence of elongated MnS particles, with lengths falling between 2 and 10 μm, together with AlN particles 4 to 6 μm in diameter. According to Humphreys,[25] the critical diameter for PSN is in the range 2 to 4 μm in 70 pct cold-rolled materials. Because this critical diameter is exceeded by the particle size distribution pertaining to a material similar to the one investigated here, PSN can be considered to play a role in the recrystallization of NO steels.

The experimental results were reproduced here by including a retained rolling texture (with a weight of 33 pct) in the nucleation texture. This suggests that PSN is not the only nucleation mechanism that is active. According to Lefever *et al.*,[26] who studied orientation selection on a similar NO steel by means of the electron backscattering pattern (EBSP) technique, the occurrence of a stored energy dependent nucleation mechanism can definitely be discerned. They observed that a low energy mechanism dominates nucleation during the early stages of recrystallization, while a high energy mechanism takes over during the later stages.

Comparison of the Taylor factor map of Figure 8 with the measured annealing textures (which reveals orientations belonging to the low as well as the high Taylor factor regions, Figure 3(c)) indicates that the observed texture development is difficult to explain in terms of a single energy dependent nucleation criterion of the type described by Eq. [6]. Given the complex nature of the successive nucleation phenomena, the present simple description of the nucleation ODF can be interpreted as providing a *mean* texture, which averages out the effects of the successive stages of nucleation.

2. *Low stored energy nucleation*

In contrast to the first rolling and annealing treatment, it is much easier to understand the nucleation texture produced by the second rolling and annealing treatment. In this case, the nucleation phenomenon is clearly dominated by the low stored energy mechanism, which is expressed here in terms of a Taylor factor dependent nucleation criterion. Several variants of such a criterion were tested, all described by expressions of the type given by Eq. [6]. In-

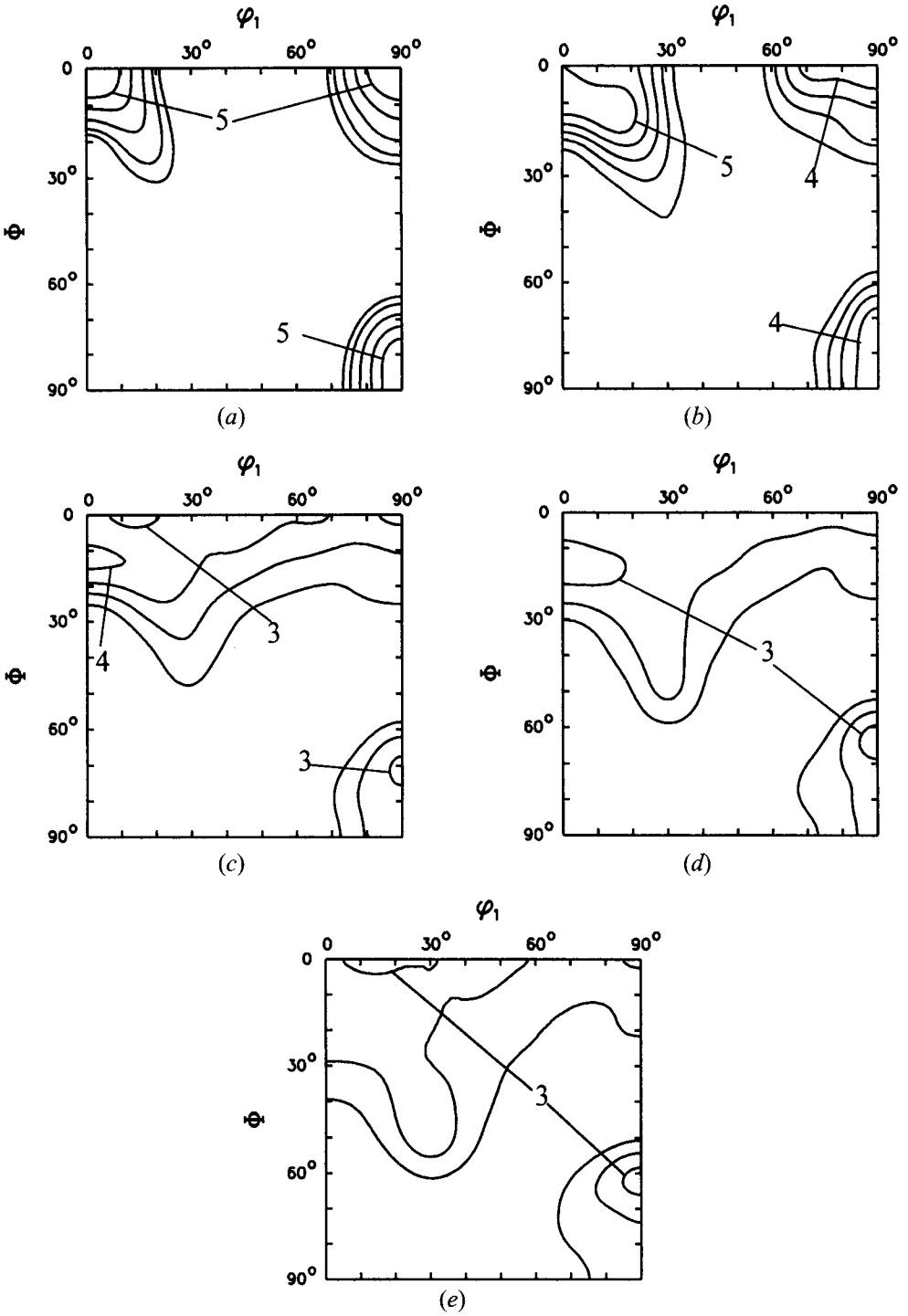

Fig. 10—Annealing texture simulated by means of Eq. [4] (with $p = 1$) and Eq. [5] (with $\theta_0 = 2$ deg and $\omega_0 = 20$ deg). The nucleation textures were obtained by employing Eqs. [2] and [6] with $M_0 = 2.3$, 2.5, 2.7, 3.0, and 3.3 in (a) through (e), respectively (levels: 1-2-3-4-5-6).

cluded were relations in which the nucleation probability $P_N(g)$ is assumed to be proportional to $(M_0 - M)^m$ (with m = an integer exponent and $M < M_0$). In these trials, the single threshold criterion of Eq. [6] led to the best agreement with the experimental texture (*cf* Figure 5(b)).

Microstructural evidence of the bulging mechanism, however, is difficult to obtain by means of optical microscopy because the phenomenon involved can only be revealed on the scale of the substructure. The low stored energy mechanism of nucleation was, therefore, confirmed in an alternative way by means of local orientation measurements carried out on the samples that were extracted from the salt bath at 730 °C after various annealing times. The orientation distribution of 95 recrystallized grains of the sample that was annealed for 4 minutes (after rolling to 5.2 pct reduction) is presented in Figure 11. It specifies the orientations that are present in the early stages of recrystallization (*cf* the micrograph of Figure 4(a)). This ODF reveals the presence of two maxima in the nucleation texture, one on the RD fiber and the other on the transverse direction (TD) fiber, in good correspondence with the predictions of the present low stored energy nucleation criterion (*cf* Figure 9).

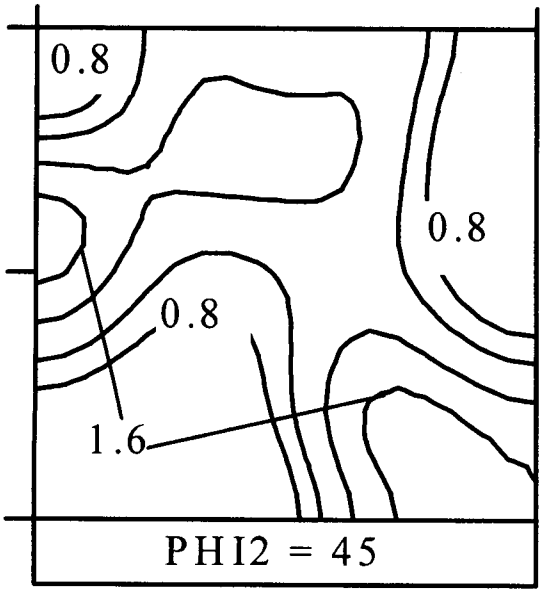

Fig. 11—EBSP texture obtained by the local orientation measurement of 95 recrystallized grains on a sample annealed for 4 min at 730 °C[14] (levels: 0.8-1.0-1.3-1.6).

Table II. Misorientation Angle Ranges of Selected Σ<110> Type CSL Boundaries

CSL Classification	Misorientation Axis	Misorientation Angle ($\omega_{\Sigma n}$)	Misorientation Range ($2\Delta\omega_{\Sigma n}$)
Σ9	<110>	38.9 deg	33.9 deg to 43.9 deg
Σ11	<110>	50.5 deg	46.0 deg to 55.0 deg
Σ17*c*	<110>	86.6 deg	82.9 deg to 90.0 deg
Σ19*a*	<110>	26.5 deg	23.1 deg to 30.0 deg
Σ33*a*	<110>	20.1 deg	17.4 deg to 22.7 deg
Σ33*c*	<110>	59.0 deg	56.4 deg to 61.6 deg

B. *Selective Growth*

Despite all the different criteria employed to model the nucleation texture, neither of the annealing textures (Figures 3(c) and 5(b)) could be reproduced solely on the basis of oriented nucleation. For this reason, calculations were carried out in both cases using selective growth combined with oriented nucleation. The textures of Figures 7 and 10 show that reasonable predictions can be produced when orientation selection plays a role during both nucleation and growth. In the course of annealing, after both 70 and 5.2 pct reduction, growth competition gives rise to slight, but nevertheless significant, morphological changes in the recrystallization texture. For the 70 pct cold-rolled sheet, selective growth is responsible for shifting the absolute maximum, along the RD fiber, from the rotated cube position (at $\Phi = 0$ deg) to $\Phi \approx 10$ deg. This leads to good agreement with the experiment, as the observed maximum was located at $\Phi \approx 5$ deg. An additional consequence of selective growth is that a secondary maximum appears on the RD fiber at $\Phi = 55$ deg ($\{111\}\langle 110\rangle$), which is also observed in the experimental texture (*cf* Figure 3(c)).

For various types of low and extra-low carbon steels, including NO electrical steels, it was argued by Lefever *et al.*,[26] Vanderschueren,[27] and Vanderschueren *et al.*[28] that the nuclei generated in particular matrix grains during the first stage of recrystallization only grow within the crystallite volumes circumscribed by the original grain boundaries. This leads to the appearance of typical elongated colonies of recrystallized grains during the first stages of recrystallization. Only toward the end of recrystallization, when the recrystallized volume fraction exceeds 50 pct, do the nuclei break out of the parent matrix grains and consume the surrounding matrix grains.

The type of selective growth modeled here only describes the orientation selection taking place during these later stages of recrystallization. This may be why it has only a minor influence on the recrystallization texture. The higher driving force provided by the high energy substructure in the parent grain (as opposed to the lower energy substructure in the *neighboring* grain) may be the decisive factor that determines the initial growth direction of the nuclei. In future modeling of selective growth, it, therefore, seems desirable to take into account the orientation dependence of the driving force P and not only the orientation dependence of the boundary mobility m (as was done in this work). (The two factors taken together make up the boundary migration velocity $v = mP$.)

C. *Role of Particular Coincident Site Lattice Boundaries*

A particular problem arises with respect to the annealing texture of the lightly rolled material. The *best* simulation result, shown in Figure 10(b) and obtained by employing the $\{110\}$ plane matching (PM) selective growth law (Eq. [5]), is not truly satisfactory. Its main defect is that it does not respect the observed intensity balance between the two maxima. In the measured texture (Figure 5(b)), the absolute maximum is at $\{441\}\langle 118\rangle$ (on the TD fiber), while the maximum in the vicinity of the RD fiber is of only secondary importance. In the simulated texture of Figure 10(b), exactly the opposite is seen. This problem cannot be solved by varying the growth amplification exponent p in Eq. [4].

In order to overcome this problem, a CSL-based growth law was also employed in the case of the lightly rolled steel. Instead of selecting for fast growth all orientation relationships based on a common $\langle 110\rangle$ axis (*i.e.*, the $\{110\}$ PM growth criterion described above), only the orientation relationships for which the rotation angle ω falls in an appropriate range are favored. The CSL boundaries that were considered in this study are listed in Table II. Each exact CSL position $\omega_{\Sigma n}\langle 110\rangle$ was relaxed according to the Brandon criterion.[29] Under these conditions, the criterion for selective growth can be expressed as follows:

$$|\omega - \omega_{\Sigma n}| > \Delta\omega_{\Sigma n} \quad P_L(\Delta g_{ij}) = 0$$
$$|\omega - \omega_{\Sigma n}| \leq \Delta\omega_{\Sigma n} \quad P_L(\Delta g_{ij}) = c_5 \exp\left[-\left(\frac{\theta_{ij}}{\theta_0}\right)^2\right] \qquad [7]$$

In Eq. [7], $\omega_{\Sigma n}$ refers to the exact Σn CSL angle (*cf* Table II) and $\Delta\omega_{\Sigma n}$ defines the relaxation range called for by the Brandon criterion ($\Delta\omega_{\Sigma n} = 15$ deg/$(\Sigma n)^{1/2}$). All the other parameters retain the meanings of their equivalents in Eq. [5], which is replaced in this case by Eq. [7].

The results for the six CSL growth relations that were implemented here are presented in Figures 12(a) through (f). It can be seen that the Σ33*a* and Σ19*a* growth criteria

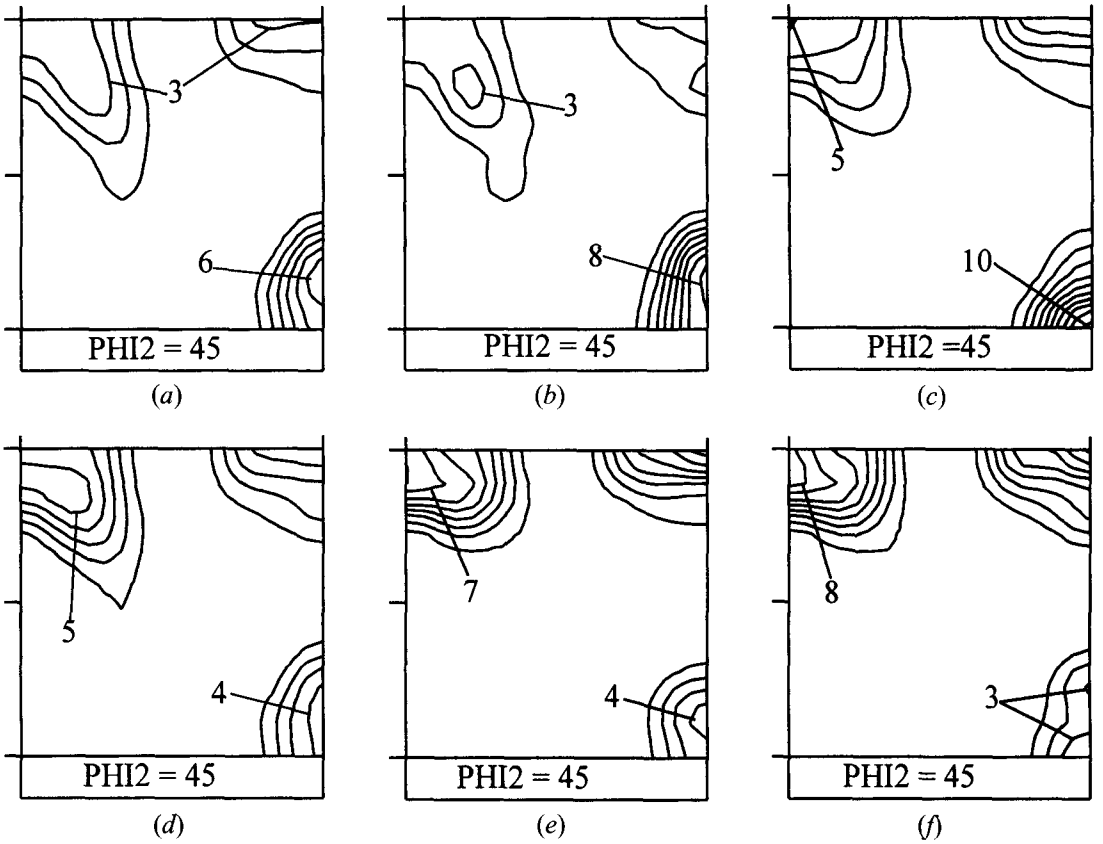

Fig. 12—Annealing texture simulated by means of Eq. [4] (with $p = 2$) and Eq. [7] (with $\theta_0 = 2$) in which ω_{Σ_n} = 20.1 deg (Σ33*a*), 26.5 deg (Σ19*a*), 38.9 deg (Σ9), 50.5 deg (Σ11), 59.0 deg (Σ33*c*), and 86.6 deg (Σ17*c*) in (a) through (f), respectively. The nucleation texture shown in Fig. 9(b) was obtained by employing Eqs. [2] and [6] with $M_0 = 2.5$ (levels: 1-2-3-4-5-6-7-8-9-10).

(*cf* Figures 12(a) and (b)) lead to an appropriate balance between the RD and TD fiber maxima. Such enhanced mobility of the 20.1 and 26.5 deg ⟨110⟩ boundaries (Σ33*a* and Σ19*a*, respectively) has already been observed in previous investigations of the recrystallization of IF steels.[12,30] The Σ19*a* (26.5 deg) simulation of Figure 12(b) is perhaps the better one, as, in this case, the secondary maximum is shifted slightly away from the RD fiber, in better correspondence with the experimental texture of Figure 5(b). The agreement with the experimental textures also extends to other (non $\varphi_2 = 45$ deg) sections of Euler space (not shown here).

The remarks made above regarding the orientation dependence of boundary mobility *m* and driving force *P* for the heavily rolled steel can now be extended to the lightly rolled material. In this case, the mobility dependence can be expected to have a more decisive effect on orientation selection than the driving force dependence. This is because there is much less stored energy in the 5.2 pct than in the 70 pct cold reduced sheet. As a consequence, the CSL dependence of the mobility is able to play a larger role. For the same reason (low density of the dislocation substructure and, thus, low value of the driving force), the variant selection criterion was abandoned in this case.

The local orientation measurements mentioned previously (*cf* Figure 11) could not be used to confirm the CSL hypothesis of selective growth. This is because they only involved the orientations of *new* grains and did not include their misorientations with respect to the surrounding matrix grains. In a similar vein, EBSP measurements on *fully recrystallized* materials cannot provide the type of nucleus/deformed matrix misorientation information needed to confirm or refute the present model. For this purpose, more detailed data, obtained at intervals during the course of recrystallization, are required. These would have to include the orientations, not only of nuclei, but also of the deformed grains into which they are growing (and which are no longer present once recrystallization is complete).

VI. SUMMARY AND CONCLUSIONS

A two-stage nucleation and growth model was employed to simulate the effect of annealing on texture development in a 70 pct and a 5.2 pct cold-rolled nonoriented electrical steel. In the nucleation stage, the texture was calculated from the experimental rolling texture by means of a suitable nucleation law; in the second stage, the nucleation texture was transformed into the recrystallization texture by the application of a suitable selective growth criterion.

The results indicate that two distinct types of nucleation occur during the processing of these steels: (a) random nucleation in the case of the sample with the conventional rolling reduction of 70 pct, in combination, perhaps, with some low and high stored energy nucleation; and (b) low stored energy nucleation in the case of the sheet that was only given a 5.2 pct reduction before annealing.

Although the main features of the recrystallization texture are predicted by the nucleation model, the fine structure of the final ODF can only be reproduced by allowing for growth

competition among the participating nuclei. In the conventionally rolled sheet, these orientation shifts can be produced by employing a growth law based on three physical features: (a) the decreased mobility of low angle grain boundaries; (b) the increased mobility of {110} plane matching boundaries; and (c) variant selection of the ⟨110⟩ axis perpendicular to the most active slip plane of the matrix grain being consumed. In the lightly rolled samples, the best correspondence with the experimental textures is obtained when the variant selection rule is abandoned and the {110} plane matching criterion is replaced by a ⟨110⟩ CSL growth criterion. Of the six CSL angles examined, the $\Sigma 19a$ (26.5 deg ⟨110⟩) and $\Sigma 33a$ (20.1 deg ⟨110⟩) orientation relationships led to the best agreement with the experimental results.

The simulations described previously demonstrate that the present nucleation and growth model can be used for the quantitative analysis of experimental textures. An attractive feature of the analysis is that it permits the individual mechanisms that are operating during orientation selective recrystallization to be determined.

ACKNOWLEDGMENTS

The authors are indebted to the N.V. Sidmar Steel Corporation (Gent, Belgium) for providing the samples for this work and to the Belgian Programme on Interuniversity Poles of Attraction initiated by the Belgian State, Prime Minister's Office, Science Policy Programming. The authors express their appreciation to Ir. Ch. Standaert and Dr. D. Vanderschueren, OCAS Research Centre (Belgium), as well as to Dr. K. Eloot and Professor J. Dilewijns, Ghent State University (Belgium), for numerous helpful discussions. Several useful discussions with Dr. P. Gangli, McGill University, are gratefully acknowledged, together with comments and suggestions received from Dr. N. Yoshinaga, Nippon Steel Corporation. Thanks are also due to Dr. J. Savoie for his assistance with the Texture Menu software developed at McGill University.

REFERENCES

1. W.B. Hutchinson: *Int. Metall. Rev.*, 1984, vol. 29, pp. 25-42.
2. N. Takahashi and J. Harase: *2nd Int. Conf. on Grain Growth (ICGG-2)*, Kitakyushu, Japan, 1995, May, pp. 143-54.
3. R.K. Ray, J.J. Jonas, and R.E. Hook: *Int. Mater. Rev.*, 1994, vol. 39, pp. 129-72.
4. L. Kestens and J.J. Jonas: *Metall. Mater. Trans. A*, 1996, vol. 27A, pp. 155-64.
5. J.J. Jonas and L. Kestens: *2nd Int. Conf. on Grain Growth (ICGG-2)*, Kitakyushu, Japan, 1995, May, pp. 155-68.
6. T. Watanabe: *Mater. Sci. Forum*, RIS0 National Laboratory, Roskilde, Denmark, 1992, vols. 94–96, pp. 209-20.
7. P.H. Pumphrey: *Special High Angle Grain Boundaries in Grain Boundary Structure and Properties*, G.A. Chadwick and D.A. Smith, eds., Academic Press, London, 1976, pp. 139-200.
8. D. Wolf: *Phil. Mag. B*, 1989, vol. 59, pp. 667-80.
9. D. Wolf: *J. Appl. Phys.*, 1991, vol. 69, pp. 185-96.
10. L.S. Tóth and J.J. Jonas: *Scripta Metall.*, 1992, vol. 27, pp. 359-63.
11. J.J. Jonas and L.S. Tóth: *Scripta Metall.*, 1992, vol. 27, pp. 1575-80.
12. T. Urabe and J.J. Jonas: *Iron Steel Inst. Jpn. Int.*, 1994, vol. 34, pp. 435-42.
13. P. Gangli, L. Kestens, and J.J. Jonas: *2nd Int. Conf. on Grain Growth (ICGG-2)*, Kitakyushu, Japan, 1995, May, pp. 667-72.
14. L. Kestens: Ph.D. Thesis, Catholic University of Leuven, Leuven, 1994, pp. 118-39 (in Dutch).
15. *P. Van Houtte: The MTM-FHM Software System*, Release 1, personal communication, Aug. 1992.
16. L.S. Tóth and P. Van Houtte: *Textures and Microstructures*, 1992, vol. 19, pp. 229-44.
17. P.A. Beck and P.R. Sperry: *J. Appl. Phys.*, 1950, vol. 21, pp. 150-52.
18. J. Savoie: *Texture Menu Software*, McGill University, Montreal, personal communication, 1994.
19. P. Van Houtte: *Textures and Microstructures*, 1988, vols. 8–9, pp. 313-50.
20. H. Inagaki: *Iron Steel Inst. Jpn. Int.*, 1994, vol. 34, pp. 313-21.
21. J. Gil Sevillano, P. Van Houtte, and E. Aernoudt: *Prog. Mater. Sci.*, 1980, vol. 25, pp. 69-412.
22. B. Hutchinson and L. Ryde: *Proc. 16th Risø Int. Symp.*, Rosklok, Denmark, (Risø National Lab., publ.) N. Hansen, D. Juul Jensen, Y.L. Liu, and B. Ralph, eds., pp. 105-17.
23. H. Inagaki: *Z. Metallkd.*, 1987, vol. 78, pp. 630-38.
24. A. De Paepe, K. Eloot, J. Dilewijns, and C. Standaert: Paper presented at SMM 12, Krakow, Poland, Sept. 1995; *J. Magn. Mater.*, in press.
25. F.J. Humphreys: *Acta Metall.*, 1977, vol. 25, pp. 1323-44.
26. A. Lefever, R. Schouwenaars, L. Rabet, P. Ratchev, P. Van Houtte, and E. Aernoudt: *Proc. 16th Risø Int. Symp.*, N. Hansen, D. Juul Jensen, Y.L. Liu, and B. Ralph, 1995, pp. 435-40.
27. D. Vanderschueren: *Proc. Int. Forum for Physical Metallurgy of IF Steels*, Iron and Steel Institute of Japan, Tokyo, 1994, pp. 145-48.
28. D. Vanderschueren, N. Yoshinaga, and K. Koyama: *Iron Steel Inst. Jpn. Int.*, 1996, in press.
29. D.G. Brandon: *Acta Metall.*, 1966, vol. 14, pp. 1479-84.
30. P. Gangli, L. Kestens, and J.J. Jonas: *Metall. Mater. Trans. A*, 1996, vol. 27A, in press.